COMPUTATIONAL MODEL OF ELECTRODE-INDUCED MICROENVIRONMENTAL EFFECTS ON pH MEASUREMENTS NEAR A CELL MEMBRANE*

DANIELA CALVETTI†, JAMIE PREZIOSO‡, ROSSANA OCCHIPINTI§, WALTER F. BORON§, AND ERKKI SOMERSALO¶

Abstract. The mechanism of gas transport across cell membranes remains a topic of considerable interest, particularly regarding the extent to which lipids versus specific membrane proteins provide conduction pathways. Studies of transmembrane carbon dioxide (CO₂) transport often rely on data collected under controlled conditions, using pH-sensitive microelectrodes at the extracellular surface to record changes due to extracellular CO₂ diffusion and reactions. Although recent detailed computational models can predict a qualitatively correct behavior, a mismatch between the dynamical ranges of the predicted and observed pH curves raises the question of whether the discrepancy may be due to a bias introduced by the pH electrode itself. More specifically, it is reasonable to ask whether bringing the electrode tip near or in contact with the membrane creates a local microenvironment between the electrode tip and the membrane, so that the measured data refer to the microenvironment rather than to the free surface. Here, we introduce a detailed computational model, designed to address this question. We find that, as long as a zone of free diffusion exists between the tip and the membrane, the microenvironment behaves effectively as the free membrane. However, according to our model, when the tip contacts the membrane, partial quenching of extracellular diffusion by the electrode rim leads to a significant increase in the pH dynamics under the electrode, matching values measured in physiological experiments. The computational schemes for the model predictions are based on semidiscretization by a finite element method and on an implicit-explicit time integration scheme to capture the different time scales of the system.

Key words. gas channels, multiscale, reaction-diffusion, anisotropy

AMS subject classifications. 35K57, 92C05, 65M60

DOI. 10.1137/19M1262875

1. Introduction. Numerous cellular processes are strongly affected by extracellular and intracellular pH, and therefore maintaining the pH values within physiological ranges is crucial for the well-being of cell functions. The central role of pH regulation makes the acid-base balance of cells a topic of wide and ongoing interest [2]. The pH inside and around a single cell depends on, among other factors, the transport of gases such as carbon dioxide (CO₂) or ammonia (NH₃) across the cell membrane. Modeling the transport of these gases is complicated by the presence of buffers surrounding the cell membrane and enzymes such as carbonic anhydrases (CAs) that effectively catalyze the interconversion of CO₂ and bicarbonate (HCO₃⁻).

^{*}Received by the editors May 20, 2019; accepted for publication (in revised form) March 16, 2020; published electronically May 28, 2020.

https://doi.org/10.1137/19M1262875

Funding: This work was partly supported by NIH grant 1U01GM111251-01 "Multi-scale Modeling of Gas Transport through Gas Channels in Living Cells." The work of the third author was supported in part by NIH grant K01 DK107787. The work of the fourth author was partly supported by ONR (N00014-15-1-2060 and MURI N00014-16-1-2535).

[†]Department of Mathematics, Applied Mathematics and Statistics, Case Western Reserve University, Cleveland, OH 44106 (dxc57@case.edu).

[‡]Department of Physiology and Biophysics, Case Western Reserve University, Cleveland, OH 44106. Current address: Metron, Incorporated, Reston, VA 20190 (jep127@case.edu).

[§]Department of Physiology and Biophysics, Case Western Reserve University, Cleveland, OH 44106 (rxo22@case.edu, wfb2@case.edu).

[¶]Corresponding author. Department of Mathematics, Applied Mathematics, and Statistics, Case Western Reserve University, Cleveland, OH 44106 (ejs49@case.edu).

In addition, the current understanding of gas transport across biological membranes points to a more complex mechanism than the traditional paradigm, in which gases dissolve in and then diffuse through lipid phase. In fact, the observation that some membranes have virtually no permeability to CO₂ or NH₃ called for alternative explanations [16]. Increasing evidence points toward certain membrane proteins such as aquaporins (AQPs) as being capable of providing a pathway, or a gas channel, for gases to pass the membrane [3, 5, 6, 7, 10, 11, 12]. The goal is to address both the extent to which these channels contribute to overall gas transport and the molecular mechanism of gas movements through these channels. However, a major challenge is that although these channels are on a nanometer spatial scale and operate on a nanosecond temporal scale, the physiological evidence is almost solely based on indirect inferences drawn from measurements on micrometer/second spatiotemporal scales. Because the extracellular and the intracellular pH are directly affected by the transport of CO₂ through the membrane, pH measurements provide the natural indirect data. Mathematical models for understanding the pH data [7, 10, 11] and for bridging the gap between the different scales have recently been developed [15, 13].

The computational models that constitute the starting point of our contribution were developed to describe CO₂ transport across the membrane of an oocyte of the African clawed frog Xenopus laevis, a spherical cell suitable for physiological studies mostly because (1) its large size (≈ 1.3 mm in diameter) allows experimental manipulations such as measurements of surface pH and (2) it is an outstanding system for the heterologous expression of the membrane proteins encoded by injection of foreign RNA [5, 12, 10, 11]. Despite the qualitative agreement between the model predictions and the measured data, the details of acid-base dynamics and transmembrane CO₂ transport are not completely resolved, as the pH dynamics is known to be sensitive to numerous factors besides the permeability of the membrane. These other factors include catalysis by CAs near or at the cell membrane, the mobility of H⁺, CO₂, and various acid-base buffers within the poorly understood fine structure of the cytoplasm inside the cell, and the vitelline membrane near the outer surface of the cell membrane. Current computational models [15, 13], while qualitatively predicting the pH dynamics observed experimentally, are unable to reproduce the dynamical range of the pH measured on the cell membrane, suggesting that the models are missing some important factors. In particular, it is possible that the exclusion of the pH electrode itself from the current models is a major contributing factor for the discrepancy. The objective of this article is to investigate, by means of a new, more detailed computational model, whether and to what extent the presence of the electrode used for measuring the pH at the membrane may create a local microenvironment that could affect the data.

The mathematical description of the experimental setting of our model is relatively straightforward: The CO₂ concentration outside a cell is regulated, and the observed pH near the cell membrane is governed by a classical reaction-diffusion equation accounting for the transport of CO₂ through the membrane. While the oocyte itself can be modeled by spherical geometry, the presence of the electrode near the membrane breaks the spherical symmetry. From the computational point of view, the submicron distance of the tip of the electrode from the membrane becomes quite challenging, because a dense spatial discretization is needed in the proximity of the electrode tip to provide useful spatial resolution. In addition, the presence of characteristic times differing by orders of magnitude renders the computational task a multiscale problem also in the temporal direction. While the individual modules of the computational model are fairly straightforward, e.g., finite element semidiscretization

and stiff time integrators, the real challenge was to bridge the orders of magnitude differences in both space and time, with slow reactions coupled to near instantaneous ones, and the state of a submicron environment linked to that of the distant free membrane. In section 2, we set up the spatially discretized model based on a finite element method (FEM), and in section 3 we propose a multiscale time integration scheme based on an implicit-explicit method. In section 4 we present computed experiments where we investigate to what extent the changes in the model's geometry alone can yield predictions that match the data, and consider two different limited diffusion scenarios. We find that, with an appropriate limitation of the diffusive accessibility of the special environment under the electrode, our new model produces pH dynamics well within the observed experimental dynamical range.

2. Reaction-diffusion model. In this section, we develop the mathematical reaction-diffusion model describing the experimental arrangement near the electrode tip in the vicinity of the cell membrane. We consider an oocyte immersed in a liquid in which the pH depends on the components of the $\rm CO_2$ buffer system and other buffers. More precisely, the bidirectional reactions affecting the pH in the liquid and inside the cell are given by

(2.1)
$$CO_2 + H_2O \underset{k_{-1}}{\overset{k_1}{\rightleftharpoons}} H_2CO_3,$$

(2.3)
$$\mathrm{HA}_{\ell} \mathop{\Longrightarrow}_{\substack{k_{-(2+\ell)} \\ k_{-(2+\ell)}}} \mathrm{A}_{\ell}^{-} + \mathrm{H}^{+}, \quad 1 \leq \ell \leq L,$$

where A_{ℓ}^- is a buffer different from the HCO $_3^-$. In this paper, we limit ourselves to the case of one nonspecified buffer, that is, L=1; thus, excluding the water, the total number of substances is N=4+2L=6. Throughout the paper, we use the following numbering for the concentrations:

$$u_1 = [CO_2], \quad u_2 = [H_2CO_3], \quad u_3 = [HCO_3^-], \quad u_4 = [H^+], \quad u_5 = [HA], \quad u_6 = [A^-].$$

In addition to the reactions above, the local concentrations change also due to diffusion and gas transport through the cell membrane, the overall dynamics being a consequence of these phenomena and the external CO₂ control. The geometric setting of the measurement is shown schematically in Figure 1.

2.1. Radial model. We start by reviewing the experimental setup and the spherically symmetric model that does not take into account the symmetry break and the possible effect of the electrode on the data.

Let R>0 denote the radius of the oocyte, assumed to be spherically symmetric, immersed in quiescent liquid. We assume that at the beginning of the experiment, the concentrations u_{ν} , $1 \leq \nu \leq N$, are constants throughout the liquid, and possibly different constants inside the cell. Further, we assume that at a distance $R_{\infty} > R$ from the center of the cell, the external concentrations are kept at constant values throughout the experiment, thus defining a constant Dirichlet boundary condition.

Denoting by u_{ν}^{+} the ν th concentration outside the cell, $R < r < R_{\infty}$, and by u_{ν}^{-} the concentration inside the cell, $0 \le r < R$, in the radial model we assume that the functions u_{ν}^{\pm} depend only on time and the radial variable r and satisfy the radial

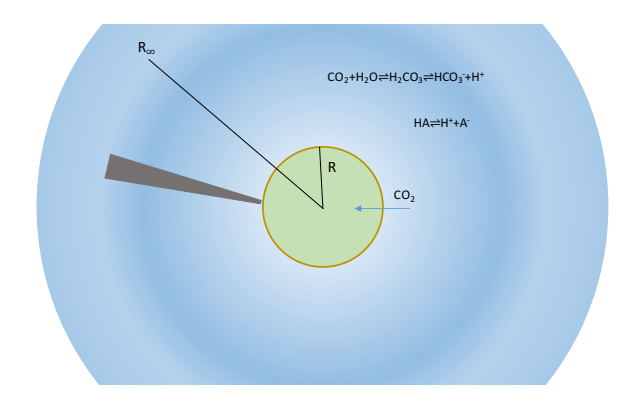


FIG. 1. The measurement geometry. The pH electrode is placed on or near the spherical oocyte immersed in a liquid in which the concentrations are controlled. The radius of the oocyte is denoted by R, while R_{∞} denotes the distance beyond which we assume that the concentrations take on prescribed constant values (i.e., those of the bulk extracellular fluid). The liquid is assumed to be quiescent; hence the reaction-diffusion equation contains no advection term.

reaction-diffusion equation,

(2.4)
$$\frac{\partial u_{\nu}^{\pm}}{\partial t} = \frac{1}{r^2} \frac{\partial}{\partial r} \left(\kappa_{\nu}^{\pm} r^2 \frac{\partial u_{\nu}^{\pm}}{\partial r} \right) + \sum_{\mu=1}^{N} S_{\nu\mu} \Phi_{\mu}^{\pm},$$

where κ_{ν}^{\pm} is the radial diffusion coefficient of the species, $S_{\nu\mu}$ is the stoichiometric matrix corresponding to the reactions (2.1)–(2.3), and Φ_{μ}^{\pm} is the reaction flux of the μ th reaction. We use the simple mass action formulas for the reactions,

where we suppressed the superscript " \pm " of the reaction fluxes, reaction rates, and concentrations. However, observe that the reaction rates $k_{\pm\ell}$ need not be the same inside and outside the cell and may vary depending on the distance from the membrane, modeling the fact that the membrane and a surrounding region may express enzymes such as CA catalyzing the reactions. These points will be detailed in the computed examples.

Finally, the exterior and interior solutions are glued together through the membrane by Fick's law,

$$\kappa_{\nu}^{+} \frac{\partial u_{\nu}^{+}}{\partial r}(R+) = \lambda_{\nu} \left(u_{\nu}^{+}(R+) - u_{\nu}^{-}(R-) \right) = \kappa_{\nu}^{-} \frac{\partial u_{\nu}^{-}}{\partial r}(R-), \quad 1 \leq \nu \leq N,$$

where λ_{ν} is the membrane permeability for the substance in question. For substances not passing through the membrane, we set $\lambda_{\nu} = 0$. For later reference, we denote the solutions of this radial system by $u_{\text{rad},\nu}^{\pm}$.

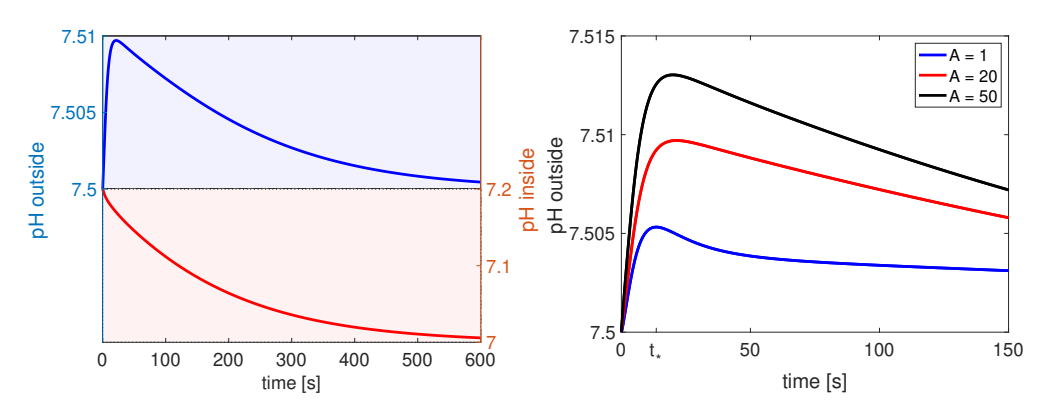
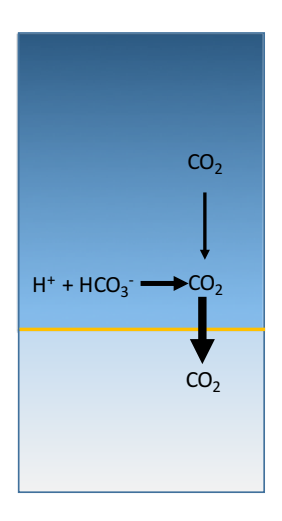


Fig. 2. Left panel: The pH on the outer surface (blue) and inner surface (red) of the cell membrane as a function of time, computed by using the radial FEM algorithm. In this simulation, the CA enhancement at the cell membrane and inside the cell is A=20. Observe the different scale on the left and on the right. Right panel: The pH curve outside the membrane corresponding to three different A values. The time t_* is when the diffusion becomes dominant compared to the transport through the membrane, and the pH starts to decrease. (Color available online.)

In [15], the radial model was studied by using a finite difference discretization of the spatial derivatives, and a standard stiff implicit solver (Runge–Kutta with backward differentiation formula) was used for solving the resulting time-dependent initial value problem. While the qualitative behavior of the solution was found to correspond well to the measured pH traces inside and outside the cell, the surface pH was unable to reproduce the dynamical range of the observations. Figure 2 shows characteristic pH curves obtained by a finite element discretization of the system (2.4) outside and inside the cell membrane (left), as well as with varying CA-induced accelerating factors of the reaction rates $k_{\pm 1}$ near the membrane outside the cell. While increasing the CA factor makes the pH peak higher, the predicted values do not match the measured data.

Figure 3 explains schematically the pH dynamics: for $t < t_*$, where t_* is the pH peak time, the system is dominated by the transport across the cell membrane, while for $t > t_*$, the transport through the membrane slows down, making the system diffusion dominated. This observation is, in some sense, the key to the modeling problem considered in this work. More precisely, we ask whether the electrode used to measure the pH creates a microenvironment near the cell membrane causing a shift of the equilibrium away from diffusion dominance, and a pH increase beyond the value reached near a free membrane. As the electrode is not likely to affect the membrane properties or reaction rates, a plausible explanation is that the replenishment of CO_2 through diffusion is affected. We therefore need to focus on the diffusion process.

2.2. Electrode geometry. To investigate the local effects of the electrode tip at or in the vicinity of the cell membrane we restrict our model to a small portion of space near the oocyte membrane containing the electrode, connecting the local model inside the domain to the exterior domain through an approximate boundary condition. Ignoring the local curvature of the cell membrane, we set the system of cylindrical coordinates (ρ, θ, z) so that the cell membrane coincides locally with the plane z = 0, and the positive direction of the z-axis, coinciding with the electrode axis, points toward the exterior of the cell. As in the radial model, the membrane thickness is assumed to be negligible, the thickness contributing to the effective permeability.



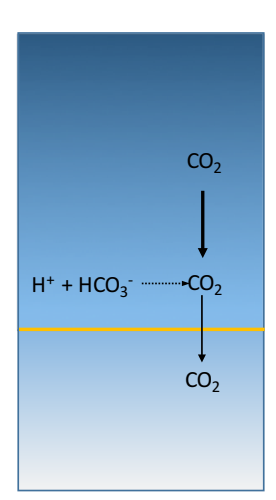


FIG. 3. Left panel: During the interval $0 < t < t_*$, the CO₂ concentration inside the cell is low, and due to the high gradient across the membrane, the transport through the cell membrane, compared to the replenishment of CO₂ through diffusion, is fast enough to guarantee that the equilibrium of the composite reaction conversion CO₂ \rightleftharpoons H⁺ + HCO₃ is strongly toward CO₂, causing an increase in pH. Right panel: As $t > t_*$, the increase in CO₂ concentration inside the cell decreases the gradient across the membrane and consequently slows down the transport rate, so that the system becomes diffusion dominated, causing the pH to drop.

The electrode tip is modeled as a rotationally symmetric cylinder along the radial axis. The sensor surface at the tip of the electrode is, in the first approximation, assumed to be flat and parallel to the membrane at a distance h > 0. We restrict the computation domain to the pillbox centered at the origin of radius W > 0, and with vertical extension $-L^- < z < L^+$, schematically shown in Figure 4. We denote by V^+ and V^- the spatial computational domains above and below the membrane, respectively, and define the two-dimensional sectorial projections Ω^{\pm} via the relation

$$V^{\pm} = \{ (\rho, \theta, z) \mid (\rho, z) \in \Omega^{\pm}, 0 \leq \theta < 2\pi \}, \quad \Omega^{\pm} \subset \mathbb{R}_{+} \times \mathbb{R}.$$

Moreover, we denote the electrode surface by Γ_e , the top and bottom surfaces of the pillbox by Γ_t and Γ_b , respectively, the outer hull $\rho = W$ of the cylinder by Γ_W , and the membrane patch inside the pillbox domain, separating V^+ from V^- , by Γ_m .

2.3. Diffusion model. Our model assumes that the diffusion processes of different species are uncoupled; therefore the corresponding governing equations can be derived for each concentration separately.

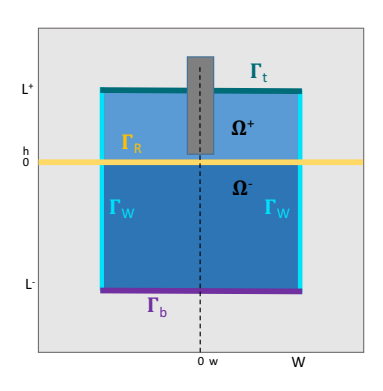
Consider a single species with concentration u = u(t, x) and let

$$u^+ = u|_{V^+}, \quad u^- = u|_{V^-}.$$

Ignoring for the time being the reaction terms, the concentrations satisfy the diffusion equation,

$$\frac{\partial u^{\pm}}{\partial t} = \nabla \cdot (\kappa \, \nabla u^{\pm}),$$

where the diffusion tensor, or mobility tensor $\kappa \in \mathbb{R}^{3\times 3}$ of the substance may depend on the position, $\kappa = \kappa(x)$; in particular, the diffusion coefficient can be different inside



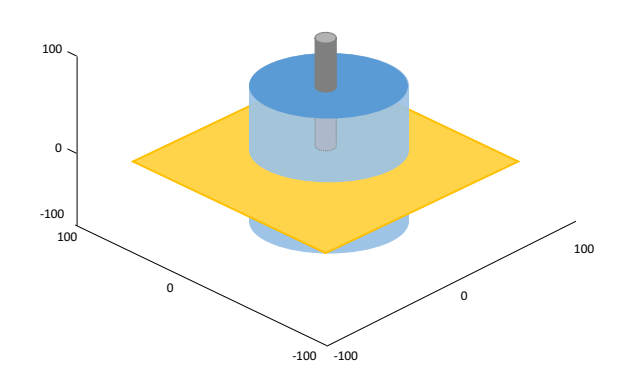


FIG. 4. A schematic picture of the geometry of the computational domain around the tip of the electrode. The yellow surface at z=0 corresponds to the cell membrane. The top and bottom surfaces at $z=\pm L^\pm$ are denoted by $\Gamma_{\rm t}$ and $\Gamma_{\rm b}$, respectively, and $\Gamma_{\rm W}$ is the cylindrical outer surface. The radius of the electrode tip is denoted by w. The proportions in this figure do not correspond to values used in the computations. (Color available online.)

and outside the cell. On the surface of the electrode, we impose the homogeneous Neumann boundary condition,

$$n \cdot \kappa \nabla u^+ \big|_{\Gamma_e} = 0,$$

where n = n(x) is the exterior unit normal vector of V^+ at the boundary.

We postulate Dirichlet data at the exterior surfaces Γ_t , Γ_b , and $\Gamma_W^{\pm} = \Gamma_W \cap \overline{V}^{\pm}$:

(2.6)
$$u^{+}|_{\Gamma_{t}} = u_{\text{out}}, \quad u^{+}|_{\Gamma_{b}} = u_{\text{in}}, \quad u^{\pm}|_{\Gamma_{W}^{+}} = u_{W}^{\pm}.$$

The boundary values u_{out} , u_{in} , and u_W^{\pm} are, in general, time dependent and will be specified later.

At the cell membrane $\Gamma_m = \{(\rho, \theta, z) \mid z = 0\}$, the interior and exterior solutions are coupled by Fick's law,

$$(2.7) -n \cdot \kappa \nabla u^{+}|_{\Gamma_{m}} = \lambda (u^{+} - u^{-})|_{\Gamma_{m}} = n \cdot \kappa \nabla u^{-}|_{\Gamma_{m}},$$

which guarantees also the conservation of mass. Here, the conormal derivatives are exterior normal projections for the respective domains. For substances that do not pass the membrane, we set $\lambda = 0$.

2.4. Coupling through chemical reactions. We include in the model the same chemical reactions (2.1)–(2.3) as in the radial model, with the mass action dynamics (2.5). The reactions provide a coupling between the diffusion models of the individual substances. Letting $S \in \mathbb{R}^{N \times N}$ denote the stoichiometric matrix of the set of N reactions above, associated to the N species that we track in our model, the governing system of reaction-diffusion equations can be written as

(2.8)
$$\frac{\partial u_{\nu}^{\pm}}{\partial t} = \nabla \cdot (\boldsymbol{\kappa}_{\nu}^{\pm} \nabla u_{\nu}^{\pm}) + \sum_{\mu=1}^{N} S_{\nu\mu} \Phi_{\mu}^{\pm}, \quad 1 \le \nu \le N,$$

equipped with the boundary conditions introduced in subsection 2.3. We remark that while diffusion and reaction rates may be different in the domains V^+ and V^- , the stoichiometry remains unaltered.

2.5. Variational form. For the semidiscretization of the problem based on finite element approximation (see, e.g., [4] for a general reference), we derive a variational form of the system of reaction-diffusion equations. In the following, we denote by H^1 the standard Sobolev space over bounded domains with smoothness index one.

We consider first the equation in V^+ . Let $v \in H^1(V^+)$ be a test function, v = v(x), with no time dependency; multiplying both sides of (2.8) by v and integrating over V^+ , we obtain

(2.9)
$$\frac{d}{dt} \int_{V^+} v u_{\nu}^+ dx = \int_{V^+} v \nabla \cdot (\kappa_{\nu}^+ \nabla u_{\nu}^+) dx + \sum_{\mu=1}^N S_{\nu\mu} \int_{V^+} v \Phi_{\nu}^+ dx.$$

Integration by parts of the diffusion term yields

$$\int_{V^+} v \nabla \cdot (\kappa_{\nu}^+ \nabla u_{\nu}^+) dx = \int_{\partial V^+} v \, n \cdot \kappa^+ \nabla u^+ dS - \int_{V^+} \nabla v \cdot \kappa_{\nu}^+ \nabla u_{\nu}^+ dx.$$

Using the homogeneous Neumann boundary condition on the surface of the electrode, the boundary integral reduces to

(2.10)
$$\int_{\partial V^+} v \, n \cdot \boldsymbol{\kappa}^+ \nabla u^+ dS = \left(\int_{\Gamma_m} + \int_{\Gamma_W^+} + \int_{\Gamma_t} \right) v \, n \cdot \boldsymbol{\kappa}^+ \nabla u^+ dS,$$

where $\Gamma_W^+ = \Gamma_W \cap \overline{V}^+$, and by choosing the test function so that

$$v \in H^1_0(V^+, \Gamma_t \cup \Gamma_W^+) = \big\{ v \in H^1(V^+) \mid v \big|_{\Gamma_t} = v \big|_{\Gamma_W^+} = 0 \big\},$$

the second and third terms in the right-hand side of (2.10) vanish, while the membrane boundary condition (2.7) can be used to reformulate the first term. In summary, (2.9) can be written as

(2.11)

$$\frac{d}{dt} \int_{V^+} v u_{\nu}^+ dx = -\lambda_{\nu} \int_{\Gamma_m} v (u_{\nu}^+ - u_{\nu}^-) dS - \int_{V^+} \nabla v \cdot \kappa_{\nu}^+ \nabla u_{\nu}^+ dx + \sum_{\mu=1}^N S_{\nu\mu} \int_{V^+} v \Phi_{\mu}^+ dx.$$

Treating the diffusion equation in the lower half space in a similar manner and choosing $w \in H_0^1(\Omega^-, \Gamma_b \cup \Gamma_W^-)$ so that $w\big|_{\Gamma_b} = w\big|_{\Gamma_W^-} = 0$, we have

$$\frac{d}{dt} \int_{V^{-}} w u_{\nu}^{-} dx = \lambda_{\nu} \int_{\Gamma_{m}} w (u_{\nu}^{+} - u_{\nu}^{-}) dS - \int_{V^{-}} \nabla w \cdot \kappa_{\nu}^{-} \nabla u_{\nu}^{-} dx + \sum_{\mu=1}^{N} S_{\nu\mu} \int_{V^{-}} w \Phi_{\mu}^{-} dx.$$

We remark that the Dirichlet boundary conditions are still implicitly imbedded in these equations and will be discussed next.

2.6. Initial-boundary values. Corresponding to the "standard experiment" described in [15], we assume that the initial values are defined as

$$u_{\nu}^{+}(0,x) = u_{\nu,0}^{+} = \text{constant}, \quad u_{\nu}^{-}(0,x) = u_{\nu,0}^{-} = \text{constant},$$

where the constants outside the cell are the values of the concentrations in the homogeneous bath, and those inside correspond to the physiological homeostasis before immersing the oocyte in the bath. Tacitly, we assume that the pH electrode is placed in the bath prior to the onset of the experiment, thus measuring the initial pH on or near the membrane from t=0 on.

To set the Dirichlet boundary condition, we assume that the perturbation due to the electrode is local enough to justify the Dirichlet conditions

$$u_{\nu}^{+}(t,x)\big|_{x\in\Gamma_{t}} = u_{\mathrm{rad},\nu}^{+}(t,R+L^{+}), \quad u_{\nu}^{-}(t,x)\big|_{x\in\Gamma_{b}} = u_{\mathrm{rad},\nu}^{-}(t,R-L^{-}),$$

where L^{\pm} denote the distances of the top and bottom boundaries from the cell membrane; see Figure 4. Likewise, at the cylindrical boundary, we use the radial solutions as boundary data,

$$u_{\nu}^{\pm}(\rho, \theta, z)|_{\rho=W} = u_{\text{rad},\nu}(t, R+z), \quad -L^{-} < z < L^{+}.$$

The assumed symmetry implies that the concentrations u_{ν}^{\pm} are independent of the angle θ , reducing the problem to a two-dimensional one over the domains $\Omega^{\pm} \subset \mathbb{R}_{+} \times \mathbb{R}$.

2.7. Semidiscretization by finite elements. In view of the axial symmetry, we may write the solutions as $u_{\nu}^{\pm} = u_{\nu}^{\pm}(t, \rho, z)$; similarly, it is reasonable to assume that the test functions v and w depend only on ρ and z. Therefore, the contribution of the integration with respect to θ amounts to a factor 2π , and the weak form integrals over the volume and along the membrane surface reduce to a two-dimensional and a one-dimensional integral, respectively,

$$dx \to 2\pi \rho d\rho dz$$
, $dS \to 2\pi \rho d\rho$

For the sake of notational simplicity, in the following we identify the two-dimensional boundary surfaces with their one-dimensional line boundaries.

We discretize the problem by generating triangular meshes in the upper and lower half spaces separately, subsequently fitting the meshes along the membrane boundary, doubling the membrane boundary nodes. We denote by n^{\pm} the number of nodes in the mesh in Ω^{\pm} , respectively, and by p_j the nodes of the mesh. Furthermore, we define the standard nodal Lagrange basis functions ψ_j to be piecewise first order polynomials satisfying the condition $\psi_j(p_k) = \delta_{jk}$, where δ_{jk} is the Kronecker delta.

Consider first the discrete approximation of u_{ν}^+ . Let $n_{\rm f}^+$ be the number of free nodes, and $n_{\rm b}^+$ the number of the bound nodes on $\Gamma_t \cup \Gamma_W^+$, so that $n_{\rm f}^+ + n_{\rm b}^+ = n^+$. We write

$$u_{\nu}^{+} \approx \sum_{k=1}^{n^{+}} \alpha_{\nu,k}^{+} \psi_{k} = \sum_{k=1}^{n_{\rm f}^{+}} \alpha_{\nu,k}^{+} \psi_{k} + \sum_{k=n_{\rm f}^{+}+1}^{n^{+}} g_{\nu,k}^{+} \psi_{k},$$

where $g_{\nu,k}^+ = g_{\nu,k}^+(t)$ is the boundary value function (2.6) of the ν th concentration at the kth node obtained by solving the radial model. Similarly, in the lower half space,

$$u_{\nu}^{-} \approx \sum_{\ell=1}^{n^{-}} \alpha_{\nu,\ell}^{-} \psi_{\ell} = \sum_{\ell=1}^{n_{\rm f}^{-}} \alpha_{\nu,\ell}^{-} \psi_{\ell} + \sum_{\ell=n_{\rm f}^{-}+1}^{n^{-}} g_{\nu,\ell}^{-} \psi_{\ell}.$$

The spatially distributed reaction fluxes are represented in terms of the same basis functions,

$$\begin{split} & \Phi_{\mu}^{+} = \sum_{k=1}^{n_{\rm f}^{+}} \varphi_{\mu,k}^{+} \psi_{k} + \sum_{k=n_{\rm f}^{+}+1}^{n^{+}} \varphi_{\mu,k}^{+} \psi_{k}, \\ & \Phi_{\mu}^{-} = \sum_{\ell=1}^{n_{\rm f}^{-}} \varphi_{\mu,\ell}^{+} \psi_{\ell} + \sum_{\ell=n_{\rm f}^{-}+1}^{n^{-}} \varphi_{\mu,\ell}^{-} \psi_{\ell}. \end{split}$$

Choosing the test function in (2.11) to be $v = \psi_j$, $1 \le j \le n_{\rm f}^+$, so that it vanishes on the top and lateral boundaries, and dividing by the common 2π -factor, we obtain

$$\sum_{k=1}^{n_{\rm f}^{+}} \frac{d\alpha_{\nu,k}^{+}}{dt} \int_{\Omega^{+}} \psi_{j} \psi_{k} \rho d\rho dz + \sum_{k=n_{\rm f}^{+}+1}^{n^{+}} \frac{dg_{\nu,k}^{+}}{dt} \int_{\Omega^{+}} \psi_{j} \psi_{k} \rho d\rho dz$$

$$= -\lambda_{\nu} \left(\sum_{k=1}^{n_{\rm f}^{+}} \alpha_{\nu,k}^{+} \int_{\Gamma_{m}} \psi_{j} \psi_{k} \rho d\rho - \sum_{\ell=1}^{n_{\rm f}^{-}} \alpha_{\nu,\ell}^{-} \int_{\Gamma_{m}} \psi_{j} \psi_{\ell} \rho d\rho \right)$$

$$-\lambda_{\nu} \left(\sum_{k=n_{\rm f}^{+}+1}^{n^{+}} g_{\nu,k}^{+} \int_{\Gamma_{m}} \psi_{j} \psi_{k} \rho d\rho - \sum_{\ell=n_{\rm f}^{-}+1}^{n^{-}} g_{\nu,\ell}^{-} \int_{\Gamma_{m}} \psi_{j} \psi_{\ell} \rho d\rho \right)$$

$$-\sum_{k=1}^{n_{\rm f}^{+}} \alpha_{\nu,k}^{+} \int_{\Omega^{+}} \nabla \psi_{j} \cdot \kappa_{\nu}^{+} \nabla \psi_{k} \rho d\rho dz - \sum_{k=n_{\rm f}^{+}+1}^{n^{+}} g_{\nu,k}^{+} \int_{\Omega^{+}} \nabla \psi_{j} \cdot \kappa_{n}^{+} u \nabla \psi_{k} \rho d\rho dz$$

$$+\sum_{\mu=1}^{N} S_{\nu,\mu} \left(\sum_{k=1}^{n_{\rm f}^{+}} \varphi_{\mu,k}^{+} \int_{\Omega^{+}} \psi_{j} \psi_{k} \rho d\rho + \sum_{k=n_{\rm f}^{+}+1}^{n^{+}} \varphi_{\mu,k}^{+} \int_{\Omega^{+}} \psi_{k} \psi_{j} \rho d\rho \right), \quad 1 \leq j \leq n_{\rm f}^{+},$$

where

$$\nabla \psi_k = \left[\begin{array}{c} \frac{\partial \psi_k}{\partial \rho} \\ \frac{\partial \psi_k}{\partial z} \end{array} \right].$$

A similar expression can be derived for the equations in the lower half space. To express these equations in matrix form, we introduce the vectors

$$U_{\nu}^{+} = \left[\begin{array}{c} \alpha_{\nu,1}^{+} \\ \vdots \\ \alpha_{\nu,n_{\mathrm{f}}^{+}}^{+} \end{array} \right], \quad U_{\nu}^{-} = \left[\begin{array}{c} \alpha_{\nu,1}^{-} \\ \vdots \\ \alpha_{\nu,n_{\mathrm{f}}^{-}}^{-} \end{array} \right], \quad 1 \leq \nu \leq N,$$

and collect the reaction fluxes into the vectors

$$F_{\mu}^{+} = \left[\begin{array}{c} \varphi_{\mu,1}^{+} \\ \vdots \\ \varphi_{\mu,n_{\mathrm{f}}^{+}}^{+} \end{array} \right], \quad F_{\mathrm{b},\mu}^{+} = \left[\begin{array}{c} \varphi_{\mu,n_{\mathrm{f}}^{+}+1}^{+} \\ \vdots \\ \varphi_{\mu,n_{\mathrm{f}}^{+}}^{+} \end{array} \right], \quad F_{\mu}^{-} = \left[\begin{array}{c} \varphi_{\mu,1}^{-} \\ \vdots \\ \varphi_{\mu,n_{\mathrm{f}}^{-}}^{-} \end{array} \right], \quad F_{\mathrm{b},\mu}^{-} = \left[\begin{array}{c} \varphi_{\mu,n_{\mathrm{f}}^{-}+1}^{-} \\ \vdots \\ \varphi_{\mu,n_{\mathrm{f}}^{-}}^{-} \end{array} \right]$$

and the boundary values into the vectors

$$G_{\nu}^{+} = \left[\begin{array}{c} g_{\mu,n_{\rm f}^{+}+1}^{+} \\ \vdots \\ g_{\mu,n^{+}}^{+} \end{array} \right], \quad G_{\nu}^{-} = \left[\begin{array}{c} g_{\mu,n_{\rm f}^{-}+1}^{-} \\ \vdots \\ g_{\mu,n^{-}}^{-} \end{array} \right].$$

Furthermore, we define the mass matrices M^+ and $M_{\rm b}^+$ with entries

$$\left(\mathsf{M}^{+}\right)_{jk} = \int_{\Omega^{+}} \psi_{j} \psi_{k} \rho d\rho dz, \quad 1 \leq j, k \leq n_{\mathrm{f}}^{+},$$

$$\left(\mathsf{M}_{\mathrm{b}}^{+}\right)_{jk} = \int_{\Omega^{+}} \psi_{j} \psi_{n_{\mathrm{f}}^{+} + k} \rho d\rho dz, \quad 1 \leq j \leq n_{\mathrm{f}}^{+}, \quad 1 \leq k \leq n_{\mathrm{b}}^{+},$$

the substance-specific stiffness matrices K_{ν}^{+} and $K_{\mathrm{b},\nu}^{+}$ with entries

and, finally, the coupling matrices

$$\begin{split} \left(\mathsf{C}^{11}\right)_{jk} &= \int_{\Gamma_m} \psi_j \psi_k \rho d\rho, \quad 1 \leq j, k \leq n_{\mathrm{f}}^+, \\ \left(\mathsf{C}^{12}\right)_{j\ell} &= \int_{\Gamma_m} \psi_j \psi_\ell \rho d\rho, \quad 1 \leq j \leq n_{\mathrm{f}}^+, \quad 1 \leq \ell \leq n_{\mathrm{f}}^-, \end{split}$$

and

$$\left(\mathsf{C}_{\mathrm{b}}^{11} \right)_{jk} = \int_{\Gamma_m} \psi_j \psi_{n_{\mathrm{f}}^+ + k} \rho d\rho, \quad 1 \le j \le n_{\mathrm{f}}^+, \quad 1 \le k \le n_{\mathrm{b}}^+,$$

$$\left(\mathsf{C}_{\mathrm{b}}^{12} \right)_{j\ell} = \int_{\Gamma_m} \psi_j \psi_{n_{\mathrm{f}}^- + \ell} \rho d\rho, \quad 1 \le j \le n_{\mathrm{f}}^+, \quad 1 \le \ell \le n_{\mathrm{b}}^-.$$

With this notation, the diffusion equation in the upper portion of the domain can be written in matrix form as

(2.15)

$$\begin{split} \mathsf{M}^{+} \frac{dU_{\nu}^{+}}{dt} &= -\lambda_{\nu} \left(\mathsf{C}^{11} U_{\nu}^{+} - \mathsf{C}^{12} U_{\nu}^{-} \right) - \mathsf{K}_{\nu}^{+} U_{\nu}^{+} + \sum_{\mu=1}^{N} S_{\nu\mu} \mathsf{M}^{+} F_{\mu}^{+} \\ &- \lambda_{\nu} \left(\mathsf{C}_{\mathrm{b}}^{11} G_{\nu}^{+} - \mathsf{C}_{\mathrm{b}}^{12} G_{\nu}^{-} \right) - \mathsf{K}_{\mathrm{b},\nu}^{+} G_{\nu}^{+} - \mathsf{M}_{\mathrm{b}}^{+} \frac{dG_{\nu}^{+}}{dt} + \sum_{\mu=1}^{N} S_{\nu\mu} \mathsf{M}_{\mathrm{b}}^{+} F_{\mathrm{b},\mu}^{+} \end{split}$$

for $1 \le \nu \le N$. Likewise, we derive a matrix differential equation for U_{ν}^- , (2.16)

$$\begin{split} \mathsf{M}^{-} \frac{dU_{\nu}^{-}}{dt} &= \lambda_{\nu} \left(\mathsf{C}^{22} U_{\nu}^{-} - \mathsf{C}^{21} U_{\nu}^{+} \right) - \mathsf{K}_{\nu}^{-} U_{\nu}^{-} + \sum_{\mu=1}^{N} S_{\nu\mu} \mathsf{M}^{-} F_{\mu}^{-} \\ &+ \lambda_{\nu} \left(\mathsf{C}_{\mathrm{b}}^{22} G_{\nu}^{-} - \mathsf{C}_{\mathrm{b}}^{21} G_{\nu}^{+} \right) - \mathsf{K}_{\mathrm{b},\nu}^{-} G_{\nu}^{-} - \mathsf{M}_{\mathrm{b}}^{-} \frac{dG_{\nu}^{-}}{dt} + \sum_{\mu=1}^{N} S_{\nu\mu} \mathsf{M}_{\mathrm{b}}^{-} F_{\mathrm{b},\mu}^{-}. \end{split}$$

To combine the equations for the upper and lower portions of the domain, let

$$U_{\nu} = \begin{bmatrix} U_{\nu}^+ \\ U_{\nu}^- \end{bmatrix} \in \mathbb{R}^{n_{\mathrm{f}}^+ + n_{\mathrm{f}}^-}, \quad F_{\nu} = \begin{bmatrix} F_{\nu}^+ \\ F_{\nu}^- \end{bmatrix} \in \mathbb{R}^{n_{\mathrm{f}}^+ + n_{\mathrm{f}}^-},$$

and, similarly,

$$G_{\nu} = \begin{bmatrix} G_{\nu}^{+} \\ G_{-}^{-} \end{bmatrix} \in \mathbb{R}^{n_{\mathrm{b}}^{+} + n_{\mathrm{b}}^{-}}, \quad F_{\mathrm{b},\nu} = \begin{bmatrix} F_{\mathrm{b},\nu}^{+} \\ F_{\mathrm{b},\nu}^{-} \end{bmatrix} \in \mathbb{R}^{n_{\mathrm{b}}^{+} + n_{\mathrm{b}}^{-}},$$

and introduce the combined mass and stiffness matrices

$$\begin{split} M &= \left[\begin{array}{cc} M^+ & \\ & M^- \end{array} \right], \quad K_\nu = \left[\begin{array}{cc} K_\nu^+ \\ & K_\nu^- \end{array} \right], \\ M_\mathrm{b} &= \left[\begin{array}{cc} M_\mathrm{b}^+ & \\ & M_\mathrm{b}^- \end{array} \right], \quad K_\mathrm{b,\nu} &= \left[\begin{array}{cc} K_\mathrm{b,\nu}^+ \\ & K_\mathrm{b,\nu}^- \end{array} \right], \end{split}$$

as well as the coupling matrices

$$\mathsf{C} = \left[\begin{array}{cc} \mathsf{C}^{11} & -\mathsf{C}^{12} \\ -\mathsf{C}^{21} & \mathsf{C}^{22} \end{array} \right], \quad \mathsf{C}_b = \left[\begin{array}{cc} \mathsf{C}_b^{11} & -\mathsf{C}_b^{12} \\ -\mathsf{C}_b^{21} & \mathsf{C}_b^{22} \end{array} \right].$$

Furthermore, introducing the vector

$$V_{\nu}(t) = -(\mathsf{K}_{\rm b} + \lambda_{\nu} \mathsf{C}_{\rm b}) G_{\nu} + \mathsf{M}_{\rm b} \sum_{\mu=1}^{N} S_{\nu\mu} F_{{\rm b},\mu} - \mathsf{M}_{\rm b} \frac{dG_{\nu}}{dt},$$

the governing equations for the ν th substance over the entire spatial domain can be written in matrix form as

(2.17)
$$\mathsf{M} \frac{dU_{\nu}}{dt} = - \left(\mathsf{K}_{\nu} + \lambda_{\nu} \mathsf{C} \right) U_{\nu} + \mathsf{M} \sum_{\nu=1}^{N} \mathsf{S}_{\mu\nu} F_{\nu} + V_{\nu}, \quad 1 \leq \nu \leq N.$$

Finally, we combine the equations for all substances into a single expression, letting

$$\mathscr{M} = \mathsf{I}_N \otimes \mathsf{M}, \quad \mathscr{L} = \left[\begin{array}{cc} \mathsf{L}_1 & & \\ & \ddots & \\ & & \mathsf{L}_N \end{array} \right], \quad \mathsf{L}_\nu = \mathsf{K}_\nu + \lambda_\nu \mathsf{C}, \quad \mathscr{S} = \mathsf{S} \otimes \mathsf{I}_{n_{\mathrm{f}}^+ + n_{\mathrm{f}}^-},$$

where the symbol " \otimes " denotes the Kronecker product and I_N is the N-dimensional unit matrix, and writing the system of differential equations (2.17) compactly as

(2.18)
$$\mathscr{M}\frac{dU}{dt} = -\mathscr{L}U + \mathscr{M}\mathscr{S}F + V,$$

where

$$U = \begin{bmatrix} U_1 \\ \vdots \\ U_N \end{bmatrix}, \quad F = \begin{bmatrix} F_1 \\ \vdots \\ F_N \end{bmatrix}, \quad V = \begin{bmatrix} V_1 \\ \vdots \\ V_N \end{bmatrix}.$$

3. Time integration. The presence of widely different time scales in the model requires a careful numerical implementation of the time integration so that the computed solution is not dominated by amplified unstable modes. We begin by observing that dissociation reactions (2.2)–(2.3) involving H⁺ equilibrate almost instantaneously relative to the time scale of diffusion and that, while their equilibrium constants are well known, the exact time scale of the fast reactions is not. The equilibrium of the fast reactions needs to be taken into consideration when assigning the boundary conditions, too.

To address the problem of the different time scales, we introduce a fast time scale parameter $\varepsilon \ll 1$, with dimension $[\varepsilon] =$ second, and write

$$k_{\pm \ell} = \frac{1}{\varepsilon} k_{\pm \ell}^*, \quad 2 \le \ell \le L,$$

where the relative rates $k_{+\ell}^*$ are dimensionless.

Integrating systems with different well-separated time scales is a widely studied topic; see, e.g., [17]. Here, to separate the time scales, we use the particular form of the mass action equations and separate the reaction term in (2.18) into the sum of the contributions from the slow reactions (2.1) and fast reactions (2.2)–(2.3), that is,

$$\mathscr{MSF}(U) = \mathscr{M}f(U) + \frac{1}{\varepsilon}\mathscr{M}h(U).$$

Observe that since the slow reactions do not involve the proton concentration, the slow contribution is linear in U,

$$f(U) = \mathcal{K}U.$$

Moreover, the slow reactions depend only on the concentrations U_1 and U_2 (CO₂ and H_2 CO₃); therefore the matrix \mathscr{K} has a block form,

$$\mathcal{K} = \begin{bmatrix} -k_1 \mathbf{I} & k_{-1} \mathbf{I} & 0 \\ k_1 \mathbf{I} & -k_{-1} \mathbf{I} & 0 \\ 0 & 0 & 0 \end{bmatrix},$$

where $\mathsf{I} = \mathsf{I}_{n_{\mathsf{f}}^+ + n_{\mathsf{f}}^-}$, and we assume that the reaction rates are uniform over all free nodes. It is straightforward to extend this formulation to account for the presence of CA near the membrane, whose effect is locally to speed up the reactions. The input vector V can be expressed in the form

$$V = W + \frac{1}{\varepsilon}B,$$

where B accounts for the contribution from the fast reactions at the boundary.

It is clear that when ε is small, the fast term dominates the right-hand side unless the system is driven into equilibrium. Let \mathcal{M} be the *slow manifold* of the concentration satisfying the equilibrium condition

$$\mathcal{M} = \{ U \mid h(U) = 0 \}.$$

To handle the different time scales in a computationally stable manner, we employ a two phase propagation, similar in spirit to the predictor-corrector schemes employed in the IMEX (implicit-explicit) approach [1]. For simplicity, we restrict our attention

to a first order propagation scheme. Let U^n denote the current numerical approximation for the solution at $t = t_n$, and assume that the fast reactions are in equilibrium both at the free nodes and at the boundary; hence $U^n \in \mathcal{M}$. Following the IMEX approach and motivated by our assumptions about U^n , we replace the original system by the following approximation:

(3.1)
$$\mathscr{M}\frac{dU}{dt}(t_n) \approx -\mathscr{L}U_*^{n+1} + \mathscr{M}\mathscr{K}U_*^{n+1} + W(t_n) + \frac{1}{\varepsilon}\left(\mathscr{M}h(U^n) + B(t_n)\right)$$
$$= -\mathscr{L}U_*^{n+1} + \mathscr{M}\mathscr{K}U_*^{n+1} + W(t_n),$$

where the $1/\varepsilon$ term vanishes due to the assumed equilibrium at t_n . We compute the solution of this stiff system to the next time instance t_{n+1} using the implicit Euler time integrator

$$\mathscr{M}\left(U_*^{n+1}-U^n\right)=-\Delta t(\mathscr{L}-\mathscr{M}\mathscr{K})U_*^{n+1}+\Delta tW(t_n),$$

where $\Delta t = t_{n+1} - t_n > 0$, which is tantamount to solving the linear system

$$(3.2) \qquad (\mathcal{M} + \Delta t(\mathcal{L} - \mathcal{M}\mathcal{K})) U_*^{n+1} = \mathcal{M}U^n + \Delta tW(t_n).$$

Since the computed solution U_*^{n+1} at the next time step is no longer guaranteed to be on the slow manifold, we need to perform a correction step to drive the fast reactions to equilibrium. To do so, consider the dominant part of the differential equation for small ε ,

(3.3)
$$\mathscr{M}\frac{dU}{dt} = \frac{1}{\varepsilon}\mathscr{M}h(U) + \frac{1}{\varepsilon}B.$$

Reparametrizing time in (3.3) in the units τ of the small time constant ε , or, equivalently, letting $t = \varepsilon \tau$, we have

(3.4)
$$\frac{dU}{d\tau} = h(U) + \mathcal{M}^{-1}B.$$

Note that since the eigenvalues of the Jacobian of h are all nonpositive, the slow manifold is stable. We then drive the system into equilibrium, starting with the initial value \mathbf{U}_*^{n+1} . Since the fast reactions were assumed to be in equilibrium at time instant t_n , in our approximation B=0; hence the system is local, nonstiff, and can be driven to equilibrium using standard ODE solvers. The new equilibrium value is denoted by \mathbf{U}^{n+1} .

- 4. Computed examples. In this section, we describe the details of the numerical experiments as well as their outcomes. We focus on the behavior of the predicted pH curve on the cell membrane, which is directly observed by the experiments.
- **4.1. Parameters and meshes.** To run the model, the first task is to solve the radial model over a free membrane, that is, without the presence of the electrode. To set up the model, we assume a spherical oocyte with diameter 1.3 mm, surrounded by a layer characterized purely by diffusion, while outside the layer the concentrations are assumed to be constants and known. The thickness of the layer in our model is 0.15 mm, so that the diffusive computational domain is a sphere with diameter 1.6 mm. Table 1 gives the geometric parameters as well as the membrane permeability.

In the basic simulation setting, we assume that the diffusion is isotropic, each substance having its characteristic mobility, or diffusion coefficient, given in Table 2.

Table 1
Geometric parameters and membrane permeability.

R	oocyte radius	$650\mu\mathrm{m}$
R_{∞}	external radius	$800\mu\mathrm{m}$
w	radius of the electrode tip	$10\mu\mathrm{m}$
λ	membrane permeability	$34.2\mu\mathrm{m/s}$

Table 2
Diffusion coefficients κ of the substances.

Substance	Inside $[(\mu m)^2/s]$	Outside $[(\mu m)^2/s]$
CO_2	1.71×10^{3}	1.71×10^{3}
H_2CO_3	1.11×10^{3}	1.11×10^{3}
HCO_3^-	1.11×10^{3}	1.11×10^{3}
H^{+}	8.69×10^{3}	8.69×10^{3}
HA	1.56×10^{3}	1.56×10^{3}
A^-	1.56×10^{3}	1.56×10^{3}

For simplicity, we assume that the mobility of each substance is the same inside and outside the cell. This assumption may be questioned, as inside the cell the mobility can be argued to be smaller due to the presence of microstructures discussed in [14]. However, as pointed out in the aforementioned article, the mobilities do not have a significant effect on the pH curve on the cell membrane. We assume that at the cell membrane and inside the cell, the presence of CA accelerates the carbonic acid formation and dissociation, modeled by increasing the corresponding reaction rates by a multiplicative factor, $k_{\pm 1} \to A \, k_{\pm 1}, \, A > 1$. The values of the reaction rates used in the calculations are given in Table 3.

Table 3

Reaction rates. Observe that for the two fast time scale parameters, ε and ε' , the precise values in the fast/slow propagation scheme are not important, since only the ratios defining the equilibrium conditions are needed in the model. When CA is present, the reaction rates $k_{\pm 1}$ are enhanced by an acceleration factor, denoted by A.

Reaction	k_ℓ	$k_{-\ell}$	K [mM]
$CO_2 + H_2O \underset{k_{-1}}{\overset{k_1}{\rightleftharpoons}} H_2CO_3$	0.0302 [1/s]	10.9631 [1/s]	2.7547×10^{-4}
$H_2CO_3 \stackrel{k_2}{\underset{k_{-2}}{\rightleftharpoons}} HCO_3^- + H^+$	$\varepsilon = 10^{-9} \text{ [1/s]}$	ε/K_2	$K_2 = 0.2407$
$HA_{in} \underset{k=3}{\overset{k_3}{\rightleftharpoons}} A_{in}^- + H_{in}^+$	$\varepsilon' = 10^{-6} \; [1/s]$	$arepsilon'/K_{ m HA}$	$K_{\rm HA} = 7.9433 \times 10^{-5}$
$\operatorname{HA}_{\operatorname{out}} \underset{k-3}{\overset{k_3}{\rightleftharpoons}} \operatorname{A}_{\operatorname{out}}^- + \operatorname{H}_{\operatorname{out}}^+$	$\varepsilon' = 10^{-6} [1/s]$	$arepsilon'/K_{ m HA}$	$K_{\rm HA} = 3.1623 \times 10^{-5}$

The finite element mesh used for computations is a triangular mesh, and the computational domain is chosen so that $0 < \rho < 40 \mu m$, and $|z| < 60 \mu m$. We perform the experiments with three different values for the gap between the electrode and the cell membrane, $h = 0.1 \mu m$, $h = 0.2 \mu m$, and $h = 0.4 \mu m$. To generate the mesh, we discretize the computational domain so that near and on the membrane, the distance between the nodes is one-third of the smallest value of h, guaranteeing that when the distance between the electrode tip and the membrane is smallest, $h = 0.1 \mu m$, there are three element layers between the membrane and the electrode, and as many as twelve when $h = 0.4 \mu m$. The element size increases when moving away from the membrane, both outside and inside the cell domain; however, the element size is kept fixed in

Table 4

The number of nodes and elements corresponding to the different distances of the electrode tip from the membrane.

Electrode distance [μm]	Number of nodes	Number of elements
0.1	47 712	94814
0.2	51 315	102014
0.4	58 521	116414

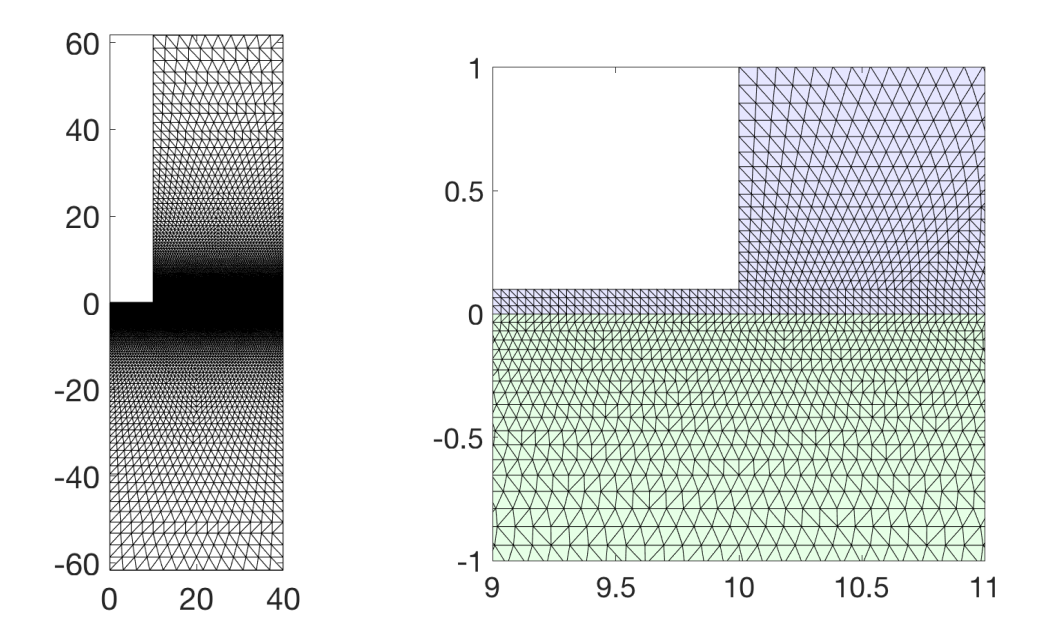


FIG. 5. The full triangular mesh used in the FEM calculation, with the electrode distance $0.1\mu m$ (left), and a detail of the mesh over a domain of size $2\times 2\,(\mu m)^2$ around the electrode corner (right). The axes are given in microns. Beyond the dense boundary layers near the membrane, the distance between the nodal layers increases geometrically by a factor 1.05 as one moves orthogonally away from the cell membrane. To guarantee isotropic elements, at each nodal layer we set the horizontal distance between nodes equal to the vertical distance between the nodal layers. The mesh is a standard Delaunay triangularization.

the layer $-0.1\mu\mathrm{m} \leq z \leq h$ along the width of the computational domain. The latter requirement implies that since the number of layers below the electrode is proportional to the distance between the tip of the electrode and the membrane, as h increases, so does the number of elements along the entire membrane, significantly increasing the number of nodes. Keeping the size of the elements the same is important because we interpolate the reaction rates linearly between nodes, and the presence of CA at the membrane nodes increases the carbonic acid formation and dissociation. Using a variable element size would cause a spatial variation in the reaction rate that cannot be justified physiologically. Despite the coarsening of the mesh in the direction away from the membrane, the required density of the mesh near the membrane leads to a large number of nodes and elements, as indicated in Table 4. Figure 5 shows the overall mesh and a detail of the mesh in the proximity of the electrode tip in the case $h = 0.1 \,\mu\mathrm{m}$. The number of variables in the system varies from 286 272 for h = 0.1 to 351 126 for h = 0.4.

Table 5

Initial values of the concentrations in the standard experiment. The model assumes that at t = 0, the oocyte is added to the bath with the pH electrode already in place.

Substance	Inside [mM]	Outside [mM]
CO_2	0	0.4720
H_2CO_3	0	0.0013
HCO_3^-	0	9.901
H^+ (pH)	$6.310 \times 10^{-5} (7.2)$	3.162×10^{-5} (7.5)
HA	12.09	2.500
A-	15.22	2.500

In the simulated protocol, referred to as "standard experiment" in [15], we assume that at t=0, the concentrations both outside and inside the cell are constants, with a concentration gradient across the membrane. In practice, we may think that the pH electrode is placed in the bath of controlled concentrations, and at t=0, the oocyte is added in the bath. The initial values of the concentrations are given in Table 5. Solutions based on the radial model with different CA enhancement values are shown in Figure 2. In the following sections, we consider the pH curve in the presence of the electrode, and with different local modifications of the mobility of the substances.

4.2. Isotropic diffusion. In the first computed protocol, we test the electrode model for three different submicron distances of the electrode tip from the membrane, setting $h = 0.4 \,\mu\text{m}$, $h = 0.2 \,\mu\text{m}$, and $h = 0.1 \,\mu\text{m}$, respectively. We assume that the diffusion processes are isotropic, thus setting

$$\kappa_{\nu} = \kappa_{\nu} I, \quad 1 \leq \nu \leq N,$$

where I is the unit matrix.

The computed pH curves are compared with the free membrane pH traces that constitute the Dirichlet boundary values at the cylindrical domain boundary Γ_W . The panels in Figure 6 show that the presence of the electrode has virtually no effect on the dynamic range of the pH at the electrode tip, or on the membrane below it, and that the distance of the electrode from the membrane does not affect significantly the response. An explanation for the lack of sensitivity to the presence and position of the electrode emerges when comparing the time constants of the different processes. Consider first the diffusion of CO_2 , whose diffusion kernel in \mathbb{R}^n , $1 \leq n \leq 3$, with diffusion coefficient κ is given by the formula

$$D(t,x) = (4\pi\kappa t)^{-n/2} \exp\left(-\frac{|x|^2}{4\kappa t}\right);$$

its characteristic diffusion time over a distance δ , regardless of the spatial dimension n, defined as the time that halves the exponential, is

$$\tau_{\rm diff} = \frac{\delta^2}{\left(4\log 2\right)\kappa}.$$

Using the radius $w = 10 \,\mu\text{m}$ as the characteristic length δ , the characteristic time for CO₂ to diffuse from the edge of the electrode to the center of the oocyte is

$$\tau_{\rm diff} \approx 0.02 \, \rm s.$$

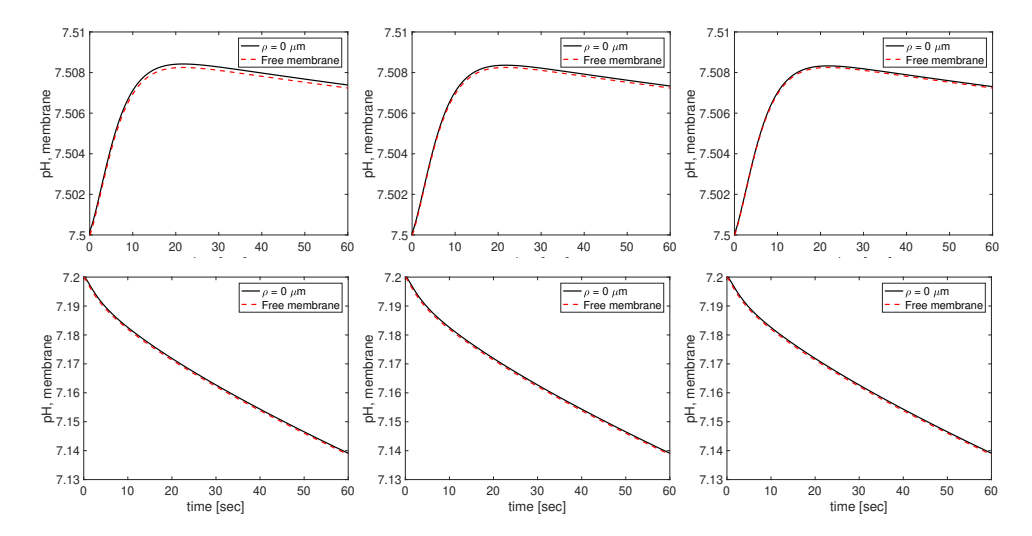


FIG. 6. The pH time courses during the first minute. The plots in the top row correspond to pH computed on the outer surface of the membrane, while those in the bottom row show the pH on the inner surface of the membrane. The dashed red curves labeled "free membrane" are the computed pH traces using the radially symmetric model where the electrode is absent. The distance of the electrode from the membrane is, from left to right, $h = 0.1 \, \mu m$, $h = 0.2 \, \mu m$, and $h = 0.4 \, \mu m$, respectively. In these experiments, the CA acceleration factor is A = 20. Thus, at the mesh nodes on the membrane and inside the cell, the reaction rates $k_{\pm 1}$ are enhanced by this factor, i.e., $k_{\pm 1} \rightarrow A \times k_{\pm 1}$. (Color available online.)

On the other hand, in the presence of CA the time constant of the slowest of the reactions, $CO_2 + H_2O \rightarrow H_2CO_3$, becomes

$$\tau_{\rm react} = \frac{1}{A \, k_1} \approx \frac{1}{A} \times 33.1 \,\mathrm{s}$$

and, even with the enhancement factor A=20, the order of magnitude of the time constant is about a second, or two orders of magnitude larger than the diffusion time. These considerations indicate that the physics is diffusion dominated, the bottleneck being the slowest reaction in the conversion chain $\mathrm{CO}_2 \to \mathrm{HCO}_3^- + \mathrm{H}^+$ affecting the pH. The reduction of the dimensionality of the special environment under the electrode from a three-dimensional space of free diffusion to an effectively two-dimensional space does not change the conclusion, as the diffusion time constant is dimension independent.

In light of the considerations above, there are two possible explanations for the putative effect of the electrode on the pH: Either the reaction rates are significantly higher in the vicinity of the membrane, or the diffusion time is significantly reduced. While the former scenario is hard to justify, the latter may be in line with the conformation of the membrane and the shape of the electrode tip. We use our model to test the second scenario in the second numerical protocol.

4.3. Anisotropic diffusion near the membrane. It is known that the cell membrane is not a smooth surface but, on the contrary, is covered by the microvilli, dense microscopic protrusions that facilitate diffusion by increasing the surface area, and various proteins attached to the membrane. Physiologically, it is therefore reasonable to assume that the diffusion in the tangential and radial directions near the membrane is different. Notice that simply lowering the scalar mobility under the

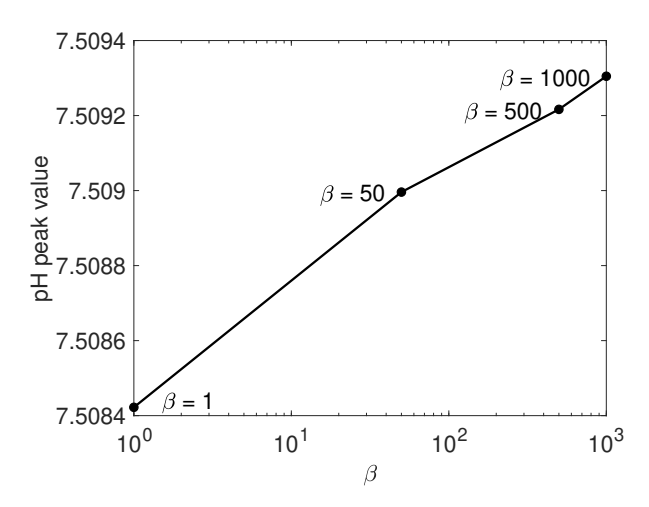


Fig. 7. The peak pH values at the membrane surface under the electrode. The tangential diffusion coefficient is reduced by a factor $1/\beta$ at the distance $z < 0.4 \mu m$ from the membrane. The CA acceleration factor is A = 20, and the distance of the electrode tip from the membrane is $0.1 \mu m$. The plot shows that the increase in the pH peak value is insignificant and increases exponentially slowly as the parameter β is increased. Observe that the increase in pH is below 10^{-3} , indicating that the anisotropy alone near the membrane is not responsible for the observable microenvironmental effect near the electrode tip.

electrode may not be justified, as the microscopic membrane structure is present in the free membrane, too, and is sometimes accounted for in the effective membrane permeability [14]. Therefore, to take into account the membrane structure, we modify the diffusion tensor near the membrane, writing it in the (ρ, z) coordinates as

$$\boldsymbol{\kappa} = \left[\begin{array}{cc} \kappa_{\rho\rho} & 0 \\ 0 & \kappa_{zz} \end{array} \right] = \kappa \left[\begin{array}{cc} 1/\beta & 0 \\ 0 & 1 \end{array} \right],$$

where κ is the scalar diffusion coefficient of the substance away from the membrane, and $\beta \geq 1$ is the slow-down factor in the direction tangential to the membrane, introduced in the space near the membrane. In our numerical experiments, we assume that $\beta = 1$ for $z > 0.4 \,\mu\text{m}$, while $\beta > 1$ in the vicinity of the membrane.

In line with the calculations of subsection 4.2, in order to render the time constants of the tangential diffusion and the reaction comparable, an enhancement factor of the order $\beta \sim 10^3$ should be introduced. However, numerical simulations shown in Figure 7 indicate that physiologically plausible reduction of the tangential mobility has only a small effect on the pH, and that the effect increases exponentially slowly as a function of the reduction factor β . We see that even a reduction by a factor of 10^3 has only a negligible enhancement effect on the peak value of the pH on the membrane below the electrode, remaining significantly lower than the reported experimental values. For this reason, a third scenario is considered.

4.4. Quenching by the electrode. The third computational protocol is designed to test the effect of the electrode rim. In the actual measurement, the electrode is not only brought close to the cell membrane but actually pushed against it, creating a dimple. While detailed modeling of this geometry would require a modification of the mesh, we may assume that effectively the electrode rim occludes the substance pathway near the edge of the electrode, leaving a partly or completely isolated pocket

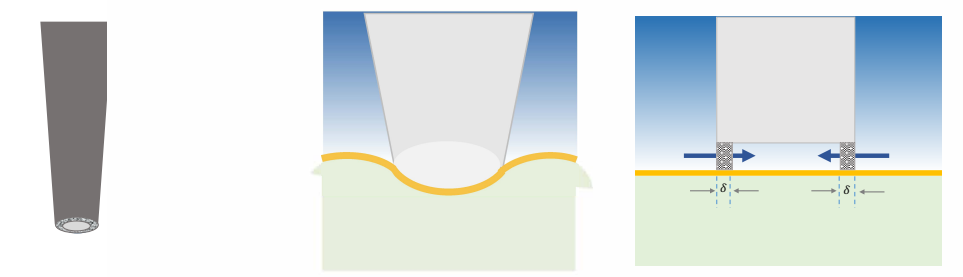


FIG. 8. Left: A schematic rendering of the geometry of the electrode tip, a micropipette with a void inside, effectively creating a partially sealed microenvironment, the level of sealing depending on the smoothness of the pipette tip [9, 8]. Middle: When the electrode is pushed against the membrane, the geometry is slightly perturbed from the horizontal structure assumed in the present model. The effect may be numerically simulated by introducing a sealing, or a rim region in which we assume that the tangential component of the diffusion tensor is locally strongly reduced, impeding the free access of the substances to the microenvironment. Right: Schematic picture of the modeling of the electrode rim effect. The horizontal mobility of the biochemical species is reduced by a factor $q \ll 1$ under the rim of thickness δ of the electrode tip, while elsewhere under the electrode the mobility is unaltered.

between the electrode and the membrane. Mathematically, this effect can be simulated by reducing the mobility over a ring of a few tenths of a micron around the electrode rim. The geometry of the modification of the model is illustrated schematically in Figure 8: We divide the domain Ω^+ into two subdomains, isolating the domain under the electrode from the exterior domain by a rim region of thickness δ where the horizontal mobility is locally significantly reduced, $\kappa_{\rho\rho} \to q\kappa_{\rho\rho}$, q < 1. We refer to q as the quench parameter. Letting q go to zero corresponds to a total occlusion by the electrode rim, creating a perfect seal approaching that obtained in patch-clamp experiments. A more realistic assumption is to use a small but positive factor q. We refer the reader to [9, 8] for a study of the effect of the electrode surface roughness. In the cited articles, it is pointed out that a smooth electrode tip considerably increases the membrane adhesion and results in improved sealing, thereby better isolating the microenvironment from the rest of the membrane.

In our computed examples we set the rim thickness to $\delta=0.1\mu\mathrm{m}$, or 1 percent of the radius of the electrode. Observe that this parameter does not represent the actual thickness of the glass of the micropipette but rather simulates the narrow contact of the outer rim with the cell membrane when the electrode is pushed against it. Figure 9 shows two pH curves on the outside surface of the membrane under the central axis of the electrode with different quench values, as well as the maximum values of the simulated pH curves, obtained by varying q over a range of values. The maxima can be well modeled by a sigmoidal function fitted to them, given by the formula

$$f(q) = \mathrm{pH_{free}} + \frac{\mathrm{pH_{sat}} - \mathrm{pH_{free}}}{1 + e^{-([-\log_{10}q] - K)/w}}, \label{eq:fq}$$

where pH_{free} = 7.508 corresponds to the maximum with no quenching, pH_{sat} = 7.780 is the saturation value, w = 0.42, and K = 5.0. Observe that while the choice of a sigmoidal model is arbitrary and the fitting of the curve is purely empirical, the upper and lower saturation values can be physically related to the limit cases with no quenching (q = 1) and completely isolated microcompartment under the electrode (q = 0).

In these simulations, we have fixed the CA acceleration factor on the membrane

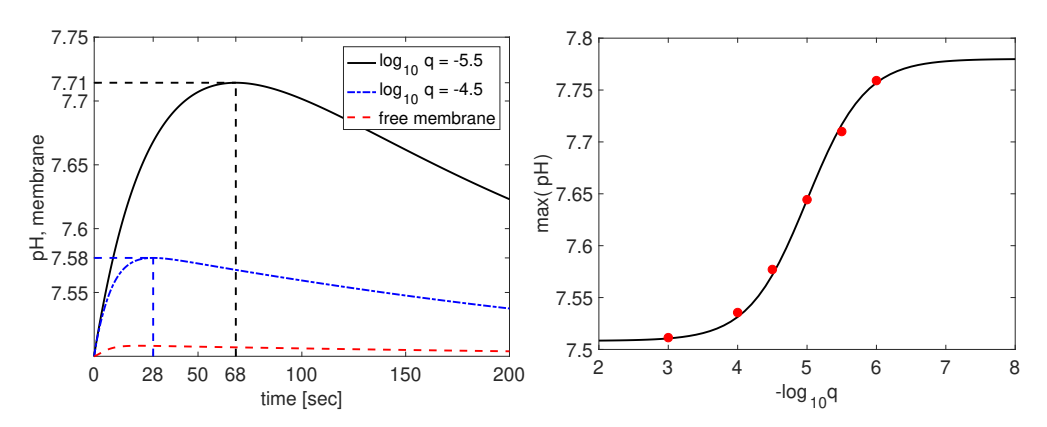


FIG. 9. Left: The pH time course on the surface of the membrane, computed with two different values of the quench parameter q. The maxima are indicated in the plot. Right: The pH maxima corresponding to different values of the parameter q, indicated by red dots, and a fitted sigmoidal curve. (Color available online.)

and inside the cell to be A = 20, and the radial mobility of the substances is otherwise unaltered, i.e., no additional anisotropy is assumed.

Quench values between $q = 10^{-4}$ and $q = 10^{-5}$ correspond to the measured dynamical range of the pH curve [11], indicating that the rim effect may indeed be a viable explanation of the discrepancy between observations and the free surface simulations.

5. Conclusions and discussion. The pH control of cells is a critically important physiological function, and transport of gases across the cell membrane plays a fundamental role in the process. A further motivation to better understand the gas transport across cell membrane comes from oxygen transport by red blood cells that need to exchange oxygen and carbon dioxide with the environment. The role of membrane proteins such as aquaporins can be studied indirectly, e.g., by pH measurements. However, the parameters describing the microstructure can be inferred from the data only if a reliable predictive model tying the two is available. In particular, it is important to understand secondary factors that may distort the model predictions and possibly lead to misinterpretations. It is a well understood principle in physics that when observing microscopic systems, the observer itself constitutes a part of the system and therefore needs to be taken into account in the model. The present article addresses this modeling challenge in the case of membrane pH measurements. Here we have shown that whereas an assumed anisotropic diffusion under the membrane (e.g., due to the presence of microvilli and various proteins protruding from the membrane) triggers only a minimal change in the pH dynamics, the quenching of diffusion by the rim of the electrode (allowing free diffusion in the pocket remaining under the electrode tip) can produce a profound effect. This quenching by the electrode rim is analogous to a leaky seal in a patch-clamp experiment. Furthermore, the maximum of the pH time course depends in a sigmoidal fashion on the logarithm of the quenching factor.

The spatial discretization in the paper is based on a first order finite element model. To gain higher accuracy, higher order schemes could be introduced, at the cost of increased computational burden. Due to computational complexity of the problem, the present article does not address in detail questions involving numerical accuracy and convergence of the discretized algorithm. Alternative approaches to increase accuracy include spectral methods and domain decomposition methods coupling the microenvironment under the electrode to the exterior domain. In this work, the primary goal was to demonstrate the existence of the electrode effect, and the development of more accurate and efficient computational schemes is left for future studies. Likewise, detailed geometric modeling of the cell membrane curvature and deformation due to the electrode, which may have a quantitative effect, are beyond the scope of the present article.

The estimation of the membrane properties, and in particular the membrane permeability from the pH data, requires the availability of a relatively fast computational model. The algorithm used in our simulations involves hundreds of thousands of unknowns and is too time consuming for solving efficiently the inverse problem of membrane permeability. Therefore, a reduced surrogate model that effectively takes into account the measuring electrode will be necessary. The sigmoidal behavior of the pH maxima may allow a way to develop a reduced model with an electrode-correction factor. The development of such a model will be the topic of future work.

Contributions of the authors. Daniela Calvetti and Erkki Somersalo were responsible for the design and implementation of the computational contents. Jamie Prezioso participated in development and testing the computational modules and running the examples. Rossana Occhipinti and Walter Boron provided physiology and biochemistry expertise needed to design the numerical methods and to interpret the results in a realistic context. All authors participated in writing the paper.

REFERENCES

- U. M. ASCHER, S. J. RUUTH, AND B. T. R. WETTON, Implicit-explicit methods for timedependent partial differential equations, SIAM J. Numer. Anal., 32 (1995), pp. 797–823, https://doi.org/10.1137/0732037.
- [2] W. F. Boron, Acid-base physiology, in Medical Physiology. A Cellular and Molecular Approach, W. F. Boron and E. L. Boulpaep, eds., Elsevier, Saunders, 2009, pp. 652–671.
- [3] W. F. Boron, The Sharpey-Schafer lecture: Gas channels, Exp. Physiol., 95 (2010), pp. 1107–1130.
- [4] S. C. Brenner and L. R. Scott, The Mathematical Theory of Finite Element Methods, 3rd ed., Texts Appl. Math. 15, Springer Science & Business Media, 2008.
- [5] G. J. COOPER AND W. F. BORON, The CO₂ permeability of the AQP1 water channel, expressed in Xenopus oocytes, J. Am. Soc. Nephrol., 8 (1997), 16A.
- [6] G. J. COOPER, R. OCCHIPINTI, AND W. F. BORON, CrossTalk proposal: Physiological CO₂ exchange can depend on membrane channels, J. Physiol., 593 (2015), pp. 5025-5028.
- [7] V. Endeward, R. Musa-Aziz, G. J. Cooper, L. Chen, M. F. Pelletier, L. V. Virkki, C. T. Supuran, L. S. King, W. F. Boron, and G. Gros, Evidence that aquaporin 1 is a major pathway for CO₂ transport across the human erythrocyte membrane, FASEB J., 20 (2006), pp. 1974–1981.
- [8] M. MALBOUBI, Y. GU, AND K. JIANG, Surface properties of glass micropipettes and their effect on biological studies, Nanoscale Res. Lett., 6 (2011), 401.
- [9] M. Malboubi, H. Ostadi, S. Wang, Y. Gu, and K. Jiang, The effect of pipette tip roughness on giga-seal formation, in Proceedings of the World Congress on Engineering, Vol. 2, 2009, pp. 801–804.
- [10] R. Musa-Aziz, L. Chen, M. F. Pelletier, and W. F. Boron, Relative CO₂/NH₃ selectivities of AQP1, AQP4, AQP5, AmtB, and RhAG, Proc. Natl. Acad. Sci. USA, 106 (2009), pp. 5406–5411.
- [11] R. MUSA-AZIZ, R. OCCHIPINTI, AND W. F. BORON, Evidence from simultaneous intracellularand surface-pH transients that carbonic anhydrase IV enhances CO₂ fluxes across Xenopus oocyte plasma membranes, Am. J. Physiol.-Cell. Physiol., 307 (2014), pp. C814–C840.
- [12] N. L. NAKHOUL, B. A. DAVIS, M. F. ROMERO, AND W. F. BORON, Effect of expressing the water channel aquaporin-1 on the CO₂ permeability of Xenopus oocytes, Am. J. Physiol., 274 (1998), pp. C543–C548.

- [13] R. OCCHIPINTI AND W. F. BORON, Mathematical modeling of acid-base physiology, Progr. Biophys. Molecular Biol., 117 (2015), pp. 43–58.
- [14] R. Occhipinti, R. Musa-Aziz, and W. F. Boron, Evidence from mathematical modeling that carbonic anhydrase II and IV enhance CO₂ fluxes across Xenopus oocyte plasma membranes, Am. J. Physiol.-Cell. Physiol., 307 (2014), pp. C841–C858.
- [15] E. SOMERSALO, R. OCCHIPINTI, W. F. BORON, AND D. CALVETTI, A reaction-diffusion model of CO₂ influx into an oocyte, J. Theoret. Biol., 309 (2012), pp. 185–203.
- [16] S. J. Waisbren, J. P. Geibel, I. M. Modlin, and W. F. Boron, Unusual permeability properties of gastric gland cells, Nature, 368 (1994), pp. 332–335.
- [17] A. ZAGARIS, H. G. KAPER, AND T. J. KAPER, Fast and slow dynamics for the computational singular perturbation method, Multiscale Model. Simul., 2 (2004), pp. 613–638, https://doi.org/10.1137/040603577.